MECHANICAL BEHAVIOR OF Be-Al ALLOYS

E. U. Lee, K. A. George, V. V. Agarwala, H. Sanders,
and G. London

Naval Air Warfare Center Aircraft Division
Patuxent River, Maryland

ABSTRACT

This study was conducted to identify the mechanical behavior of a wrought 62Be-38Al alloy and a cast 65Be-32Al-3Ni alloy. Tensile strength and elongation were measured at room and elevated temperatures. Fracture toughness was determined at room temperature. Fatigue resistance was characterized in terms of stress-life (S-N) and crack growth rate-stress intensity range (da/dN-ΔK) relations at room temperature. The resulting microstructures and crack paths of the aforementioned were also examined.

The microstructure of the wrought and cast alloys consists of Be-phase particles within an Al-phase matrix. The Be-phase particles are aligned along the rolling direction in the wrought alloy, whereas they are coarser and round with no directionality in the cast alloy. Overall, the wrought alloy has better mechanical properties, including fatigue resistance, than the cast alloy. The conditional plane strain fracture toughnesses of the wrought alloy were determined to be 38.8 and 22.4 MPa$\sqrt{m}$ (35.3 and 20.4 ksi$\sqrt{in}$) for the L-T and T-L orientations at room temperature, respectively. The crack path follows preferentially along the Al-phase and the Al/Be interfacial region for the wrought alloy at all temperatures and for the cast alloy at higher temperatures during tensile, fracture-toughness, and fatigue testing. However, while tensile testing at room temperature, the crack cuts through the Be- and Al-phases in the cast alloy.

INTRODUCTION

High specific modulus aerospace structures should have low density and good thermal conductivity to resist vibration, deformation, and high heat loads. Additional performance requirements are becoming necessary with the advent of advanced supersonic and hypersonic designs. These include high fracture toughness, fatigue resistance, strength, and ductility to eliminate or minimize the possibility of catastrophic fracture and fatigue failure, and to facilitate the weight saving and fabrication. Several material systems have been investigated for their capability in meeting the stringent combination of the aforementioned requirements, including titanium aluminide intermetallic compounds, metal matrix composites, and beryllium. However, these materials have proven to be deficient in their ability to meet the desired fracture toughness and fatigue resistance. Thus, an alloy system, combining beryllium's attributes of low density, high strength, and high modulus with aluminum's low temperature toughness, offers a viable candidate material.

Among the attributes of beryllium are its low density of 1.85 g/cm^3 (0.067 lb/in^3) and high elastic modulus of 276 to 303 GPa (40x10^6 to 44x10^6 psi). The density is approximately 2/3 that of aluminum and ¼ that of steel. This gives beryllium a specific modulus 6.6 times greater than that of aluminum, steel, magnesium, and some titanium alloys. However, beryllium has several drawbacks for its use as an aircraft material. For instance, the fracture toughness of a consolidated beryllium powder metallurgy product is lower than that of most materials, typically in the range of 7.7 to 12.1 MPa$\sqrt{m}$ (7 to 11 ksi$\sqrt{in}$). In addition, beryllium cannot be welded by conventional means. Therefore,

alloying with aluminum can improve the fracture toughness and also allow fabrication and repair of components by fusion welding.

Recently, beryllium-aluminum alloys have shown a potential for overcoming the deficiencies of beryllium. Alloys, which have undergone the most intensive prior evaluation, generally in the region of 30 to 40% aluminum (1), were found to have improved ductility and a more forgiving failure mode. In particular, the composition of 62Be-38Al has had the greatest attention within the aircraft structural alloy community (2-5). However, the improvement in room temperature elongation associated with the higher aluminum content was accompanied with a decreased strength and modulus and an increased density. Therefore, the limit of aluminum concentration of Be-Al alloys must be considered because of the increased density, reduced strength, and reduced modulus associated with the dilution of beryllium. Other investigations have concentrated upon modifications incorporating either a higher aluminum content or the addition of ternary alloying elements, most notably 53Be-47Al (LX-53) and 59Be-38Al-3Mg (LX59-3). Thus far, the use of a ternary alloying element in a lower beryllium content alloy has appeared to improve yield, ultimate tensile strength, and elongation.

Research and development efforts, performed in the 1960's and 1970's, have focused on the attributes of a uniform and fine microstructure provided by powder metallurgy (PM) technology. Investigations prior to the PM work revolved around ingot metallurgy (IM) technology (sand and mold casting) which produced a coarse dendritic structure that did not produce mechanical properties appropriate for structural components (1). By the late 1980's, the capability to manufacture wrought Be-Al alloys, using both IM and PM, was reinvestigated. Recently, a study on casting of Be-Al alloys, including 65Be-32Al-3Ni alloy, has been emphasized and conducted. Therefore, an investigation of the mechanical behavior of Be-Al alloy casting is required for the intended application. This study was initiated to identify the mechanical behavior of a representative wrought alloy, 62Be-38Al, and of a newly developed cast alloy, 65Be-32Al-3Ni.

EXPERIMENTAL PROCEDURES

The specimen materials consist of plates of wrought 62Be-38Al alloy and a bearing housing of casted 65Be-32Al-3Ni alloy. They were procured from Brush Wellman Inc. Their chemical compositions are shown in Tables 1 and 2 below.

Table 1. Chemical composition of wrought 62Be-38Al alloy

Element:	Al	Be	0	C	Other Elements, Each
Weight %	38.22	61.2	0.24	0.057	0.2 Max

Table 2. Chemical composition of cast 65Be-32Al-3Ni alloy

Element:	Al	Be	Ni	C	Cd	Fe
Weight %:	36.0	60.6	2.9	0.06	0.2	0.3

The microstructures of the specimen materials were examined with the aid of an optical microscope, Nikon Epiphot.

The specimen materials were machined into rectangular, round, and compact tension specimens.

Two closed-loop servo-hydraulic MTS mechanical test machines of 100 KN (20 kip) were employed for the tension, fracture toughness, and fatigue tests. Each machine was monitored and controlled by a computer. The tension test was performed at room temperature, 66°C (150°F), 121°C (250°F), 177°C (350°F) and 232°C (450°F) with a constant crosshead speed of 0.25 mm/min (0.01 in/min) in laboratory atmosphere. The specimens for this test were rectangular and round specimens. The fracture toughness test was done at room temperature, following ASTM Standard E 1820-96, using a compact tension specimen. The stress-life (S-N) fatigue test was performed under force controlled constant amplitude axial loading at a stress ratio 0.1 and frequency of 30 Hz at room temperature in laboratory atmosphere. The specimens for this test were rectangular and round fatigue test specimens with a continuous radius between ends. The fatigue crack growth test was conducted under a constant amplitude sine wave loading at a frequency of 30 Hz and stress ratios, ranging from 0.1 to 0.6, at room temperature in laboratory atmosphere. In this test, utilizing a compact tension specimen, the crack length was continuously monitored with a compliance measurement technique. The near-threshold crack growth rate was obtained under a decreasing stress intensity K (load shedding) condition with a K-gradient parameter $C = -0.16\ mm^{-1}$.

After each mechanical test, the fracture surface of the specimen was examined under a Scanning Electron Microscope, JEOL JSM-5800LV, operating with a 20 kV accelerating voltage. Subsequently, the fracture path was identified with an optical microscope, Nikon Epiphot.

RESULTS AND DISCUSSION

MICROSTRUCTURE

Microstructures of the wrought and cast alloys are shown in Figures 1(a) and (b). The dark color structure is the Be-phase and the light one the Al-phase matrix. Note that for the wrought alloy, the Be-phase particles are not deformed, but they are aligned along the rolling direction, resulting in banding, Figure 1(a). However, for the cast alloy, they are coarser and round or partly equiaxed with no directionality, Figure 1(b).

TENSILE PROPERTIES

Tensile test results are summarized for both the wrought and cast alloys in Table 3. Their respective stress-strain curves are shown as a function of test temperature and loading orientation in Figures 2-4. The yield strength (YS) and ultimate tensile strength (UTS) are higher at lower test temperatures, with the wrought alloy possessing superior strength and ductility than the cast alloy. In the wrought alloy, the YS and UTS are greater in the L-orientation than in the T-orientation below a test temperature of 177°C (350°F); but the reverse is true above 177°C (350°F).

Typical fracture paths are illustrated for the wrought and cast alloys that have been tensile tested in Figures 5-8. For the wrought alloy, the fracture surface is nearly perpendicular to the loading direction and planar at room temperature, Figure 5. Fracture occurs partly through the Be-phase and partly through the Al-phase and the Al/Be interfacial region at room temperature. On the other hand, at higher temperatures, the fracture surface is wavy and the fracture path follows preferentially along the Al-phase and the Al/Be interfacial region, Figure 6. Such a fracture path feature is seen for both the L- and T-loading directions. For the cast alloy, the fracture surface is slanted towards the loading direction, and the fracture path cuts through the Be- and Al-phases at room temperature, Figure 7. However, at higher temperatures, the fracture path again follows preferentially along the Al-phase and Al/Be interfacial region, Figure 8.

Table 3. Tensile properties

	Temp		YS		UTS		Elong	Modulus	
Orientation	°C	°F	MPa	ksi	MPa	ksi	%	GPa	Msi
Wrought									
L	RT		348.9	50.6	429.5	62.3	8.9	103.4	15.0
	66	150	336.5	48.8	406.8	59.0	9.2	124.1	18.0
	121	250	299.9	43.5	344.7	50.0	10.0	137.9	20.0
	177	350	276.5	40.1	299.2	43.4	8.3	95.1	13.8
	232	450	251.0	36.4	260.6	37.8	7.1	63.4	9.2
T	RT		330.9	48.0	413.7	60.0	8.7	120.7	17.5
	66	150	325.4	47.2	388.2	56.3	7.1	104.8	15.2
	121	250	303.4	44.0	344.7	50.0	7.1	112.4	16.3
	177	350	284.8	41.3	306.1	44.4	7.8	113.1	16.4
	232	450	251.7	36.5	264.1	38.3	7.3	72.4	10.5
Cast	RT		142.0	20.6	173.1	25.1	3.1	37.2	5.4
	66	150	154.4	22.4	175.8	25.5	-	49.6	7.2
	121	250	137.9	20.0	146.2	21.2	3.6	32.4	4.7
	177	350	103.4	15.0	114.5	16.6	-	29.0	4.2
	232	450	96.5	14.0	99.3	14.4	4.0	43.4	6.3

FRACTURE TOUGHNESS

The conditional plane strain fracture toughness K_Q of the wrought alloy was determined to be 38.8 and 22.4 MPa$\sqrt{m}$ (35.3 and 20.4 ksi$\sqrt{in}$) for the L-T and T-L orientations at room temperature, respectively.

The fracture path can be seen in the micrograph, Figure 9, of a side face through the fracture surface for a wrought alloy specimen. The fracture propagates through mostly the Al-phase, the Al/Be interfacial region, and some of the Be-particles for both orientations, L-T and T-L.

Figure 10 reveals the fracture surface topographies obtained by optical microscopy for the fracture-toughness-tested wrought alloy specimens of L-T and T-L orientations. Starting from the left edge (in sequence) the zones are identified as the machined notch, fatigue-pre-cracked, and radial. The fractographic features of the radial zone consist of coarse radial ridges and marks for the L-T orientation and fine radial marks for the T-L orientation. The radial ridges and marks run parallel to the direction of crack growth. (Such a ridge is created when tearing of the intermediate material connects two non-coplanar cracks). The difference in fractographic features between the L-T and T-L orientations must be associated with the large difference in fracture toughness.

The corresponding SEM fractographs and elemental (Be, Al) X-ray dot maps are shown in Figure 11. Cleavage facets are seen in the Be-phase and dimples in the Al-phase. These observations substantiate that the Be-phase fails by cleavage fracture and the Al-phase by ductile dimple fracture.

FATIGUE BEHAVIOR

The results of the stress-life fatigue test, S-N curves, are shown for both the wrought and cast alloys in Figure 12. The wrought alloy is more resistant to fatigue than the cast alloy. Furthermore, the fatigue resistance is greater in the L-orientation than in the T-orientation.

Figures 13-18 depict the typical results of the fatigue crack growth test. At R=0.1, the threshold stress intensity range ΔK_{th} is greater and the fatigue crack growth rate da/dN is lower for L-T orientation than for T-L orientation, Figure 13. On the other hand, at R=0.6, the values of ΔK_{th} and the da/dN are similar for both the L-T and T-L orientations, in the near-threshold crack growth regime, Figure 14. However, the da/dN is greater for T-L orientation than for L-T orientation in the Paris regime. For the cast alloy, ΔK_{th} is 11.1 MPa$\sqrt{m}$ (10.1 ksi$\sqrt{in}$), which is much higher than that for the wrought alloy and da/dN increases greatly with a slight increase in ΔK, Figure 15. This indicates that the threshold crack growth resistance of the cast alloy is superior to the wrought alloy, but its resistance to subsequent fatigue crack growth is inferior. Figure 16 shows the effect of stress ratio R on ΔK_{th} and da/dN for the wrought alloy. From this figure, it is evident that ΔK_{th} decreases but da/dN increases with increasing R. Similar observations have been

reported for the other metallic materials (6-11).

The variation of ΔK_{th} and maximum stress intensity $K_{max} = \Delta K_{th}/(1-R)$ with R is shown for the wrought alloy specimens of L-T orientation in Figure 17. ΔK_{th} decreases with increasing R for $R < 0.3$ and levels off for $R > 0.3$. K_{max} changes little for $R < 0.3$, but increases sharply above $R > 0.3$. ΔK_{th} is plotted against K_{max} in Figure 18. Such a curve is called a fundamental threshold curve (12), which defines regions where a fatigue crack grows (above the curve) and where it does not (below the curve). The curve in Figure 18 delineates a boundary where fatigue crack growth starts for a given K_{max} and specifies the resistance of the wrought alloy to threshold fatigue crack growth.

A typical fatigue crack path is shown in the micrograph of a section through each fracture surface for both the wrought and cast alloy specimens in Figures 19 and 20. Note that the fatigue crack propagates preferentially through the Al-phase and Al/Be interfacial region in both alloys.

CONCLUSIONS

1. The microstructures of the wrought 62Be-38Al and cast 65Be-32Al-3Ni alloys consist of Be-phase particles within an Al-phase matrix. The Be-phase particles are aligned along the rolling direction in the wrought alloy but coarser and without directionality in the cast alloy.

2. The yield and ultimate tensile strengths are greater at low test temperatures; the wrought alloy has superior strength and ductility compared to the cast alloy.

3. In the wrought alloy, tensile fracture occurs partly through the Be-phase, the Al-phase, and the Al/Be interfacial region at room temperature. However, at higher temperatures, the fracture path follows preferentially along the Al-phase and the Al/Be interfacial region.

4. In the cast alloy, tensile fracture cuts through the Be- and Al-phases at room temperature. However, at higher temperatures, the fracture path follows more preferentially along the Al-phase and the Al/Be interfacial region.

5. The conditional plane strain fracture toughnesses at room temperature for the wrought alloy are 38.8 and 22.4 MPa$\sqrt{m}$ (35.3 and 20.4 ksi$\sqrt{in}$) for L-T and T-L orientations, respectively.

6. During fracture toughness testing of the wrought alloy, the fracture propagates mostly through the Al-phase and Al/Be interfacial region, and through some Be-phase particles. The fracture mode of the Be-phase is cleavage fracture, whereas that of the Al-phase is ductile dimple fracture.

7. The wrought alloy has greater fatigue endurance than the cast alloy. It is also more

fatigue resistant in the L-orientation than in the T-orientation loading.

8. The cast alloy has a superior resistance to threshold fatigue crack growth but an inferior resistance to subsequent fatigue crack growth than the wrought alloy.

9. The fatigue crack propagates preferentially through the Al-phase and Al/Be interface region for both the wrought and cast alloys.

REFERENCES

1. R. W. Fenn, Jr., W. C. Coons, D. D. Crooks, A. S. Neiman, J. Robinson and G. H. Watts, "Evaluation of Be-38% Al Alloy," *NASA Contract NAS8-11448,* (1965).

2. F. A. Crossley and D. D. Crooks, *Lockalloy Research and Development, Final Technical Report, LMSC-D267216, Lockheed Missiles & Space Co., Palo Alto, CA,* (1972).

3. G. J. London, "Alloys and Composites - Beryllium-Aluminum Alloys," B*eryllium Science and Technology, ed. D. R. Floyd and J. N. Lowe, Plenum Press, New York, NY*, **2**, 297, (1979).

4. R. J. Duba, A. C. Haramis, R. F. Marks, L. Payne and R. C. Sessing, *YF-12 Lockalloy Ventral Fin Program, Final Report, NASA CR-144971, Lockheed-California Co., Burbank, CA,* **1** (1976).

5. G. J. London, *Beryllium-Aluminum Sheet and Tubing Development Program, NASP Technical Memorandum 1210, Naval Air Warfare Center, Warminster, PA,* (1995).

6. S. Suresh, A. K. Vasudevan, and P. E. Bretz, "Mechanisms of Slow Fatigue Crack Growth in High Strength Aluminum Alloys: Role of Microstructure and Environment," *Metallurgical Transactions A,* **15A**, 369 (1984).

7. R. J. Cooke and C. J. Beevers, "The Effect of Load Ratio on the Threshold Stresses for Fatigue Crack Growth in Medium Carbon Steels," *Engineering Fracture Mechanics,* **5** 1061 (1973).

8. R. O. Ritchie, "Near-Threshold Fatigue-Crack Propagation in Steels," *International Metals Review,* (5 and 6) 205 (1979).

9. J. L. Robinson and C. J. Beevers, "The Effects of Load Ratio, Interstitial Content, and Grain Size on Low-Stress Fatigue-Crack Propagation in α-Titanium," *Metal Science Journal*, **7** 153 (1973).

10. G. C. Salivar and J. E. Heine, "The Effect of Stress Ratio on the Near-Threshold Fatigue Crack Growth Behavior of Ti-8Al-1Mo-1V at Elevated Temperature,"

Engineering Fracture Mechanics, **32** (5) 807 (1989).

11. J. L. Yuen, P. Roy, and W. D. Nix, "Effect of Oxidation Kinetics on the Near Threshold Fatigue Crack Growth Behavior of a Nickel Base Superalloy," *Metallurgical Transactions A*, **15A** 1769 (1984).

12. A. K. Vasudevan, K. Sadananda, "Classification of Fatigue Crack Growth Behavior," *Metallurgical and Materials Transactions A*, **26A** 1221 (1995).

LIST OF FIGURES

Figure No.	Caption
1	Microstructures of wrought Be-Al and cast Be-Al-Ni alloys.
2	Stress-strain curves for wrought Be-Al alloy of L-orientation at various temperatures.
3	Stress-strain curves for wrought Be-Al alloy of T-orientation at various temperatures.
4	Stress-strain curves for cast Be-Al alloy at various temperatures.
5	Optical micrograph of a longitudinal section through the fracture surface showing the fracture path and microstructure for a wrought Be-Al alloy specimen that had been tensile tested at room temperature.
6	Optical micrograph of a longitudinal section through the fracture surface showing the fracture path and microstructure for a wrought Be-Al alloy specimen tensile tested at 232°C (450°F).
7	Optical micrograph of a section through the fracture surface showing the fracture path and microstructure for a cast Be-Al alloy specimen tensile tested at room temperature.
8	Optical micrograph of a section through the fracture surface showing the fracture path and microstructure for a cast Be-Al alloy specimen tensile tested at 232°C (450°F).
9	Optical micrograph of a section through the fracture surface showing the fracture path and microstructure for a wrought Be-Al alloy specimen of L-T orientation that had been fracture-toughness tested at room temperature.
10	Photographs depicting the fracture surfaces of wrought Be-Al alloy specimens that were fracture-toughness tested at room temperature.
11	SEM fractograph and X-ray dot maps for a wrought Be-Al alloy specimen of L-T orientation that had been fracture-toughness tested at room temperature.
12	Stress-life (S-N) curves for wrought and cast Be-Al alloys that were fatigue tested at room temperature.

13 Variation of fatigue crack growth rate da/dN with stress intensity range ΔK for wrought Be-Al alloy specimens of L-T and T-L orientations at a stress ratio R = 0.1.

14 Variation of fatigue crack growth rate da/dN with stress intensity range ΔK for wrought Be-Al alloy specimens of L-T and T-L orientations at a stress ratio R = 0.6.

15 Variation of fatigue crack growth rate da/dN with stress intensity range ΔK for a cast Be-Al alloy specimen at a stress ratio R = 0.1.

16 Variation of fatigue crack growth rate da/dN with stress intensity range ΔK for wrought Be-Al alloy specimens of L-T orientation at stress ratios R = 0.1 and 0.3.

17 Variation of threshold stress intensity range ΔK_{th} and maximum stress intensity K_{max} with stress ratio R for wrought Be-Al alloy specimens of L-T orientation.

18 Fundamental threshold curve of threshold stress intensity range ΔK_{th} vs. maximum stress intensity K_{max} for wrought Be-Al alloy specimens of L-T orientation.

19 Optical micrographs of a section through the fracture surface showing the fracture path and microstructure for wrought Be-Al alloy specimens of L-T orientations that had undergone fatigue testing at room temperature.

20 Optical micrograph of a section through the fracture surface depicting the fracture path and microstructure for a cast Be-Al-Ni alloy specimen that had undergone fatigue testing at room temperature.

LIST OF TABLES

Table No. Caption

1 Chemical composition of wrought 62Be-38Al alloy.

2 Chemical composition of cast 65Be-32Al-3Ni alloy.

3 Tensile properties.

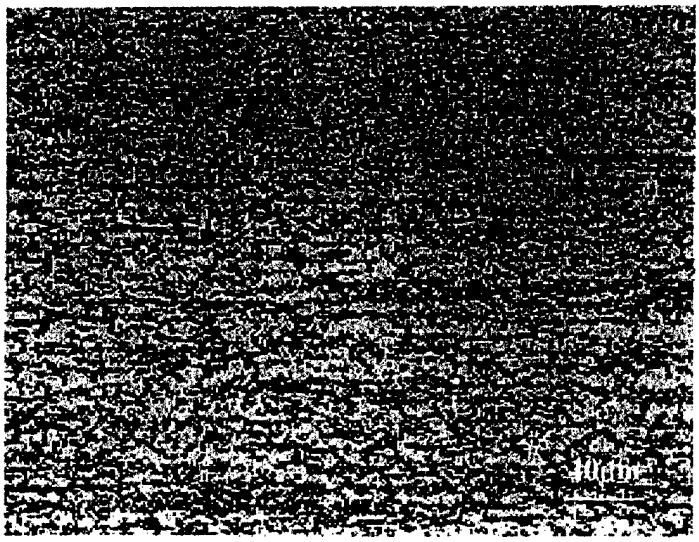

(a) Wrought alloy

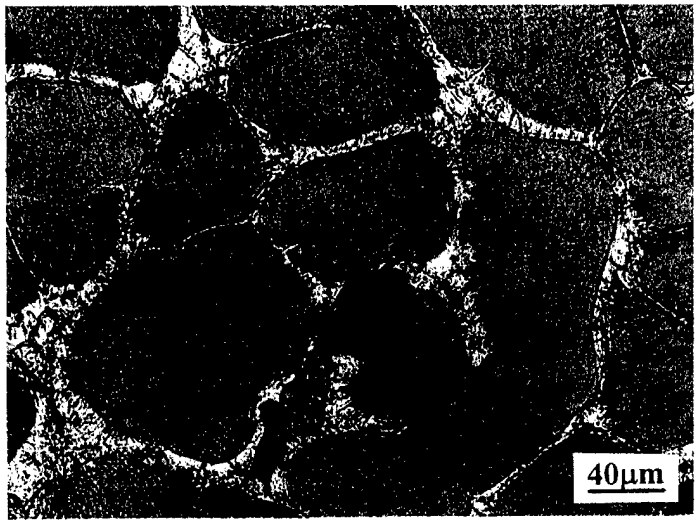

(b) Cast alloy

Figure 1. Microstructures of wrought Be-Al and cast Be-Al-Ni alloys.

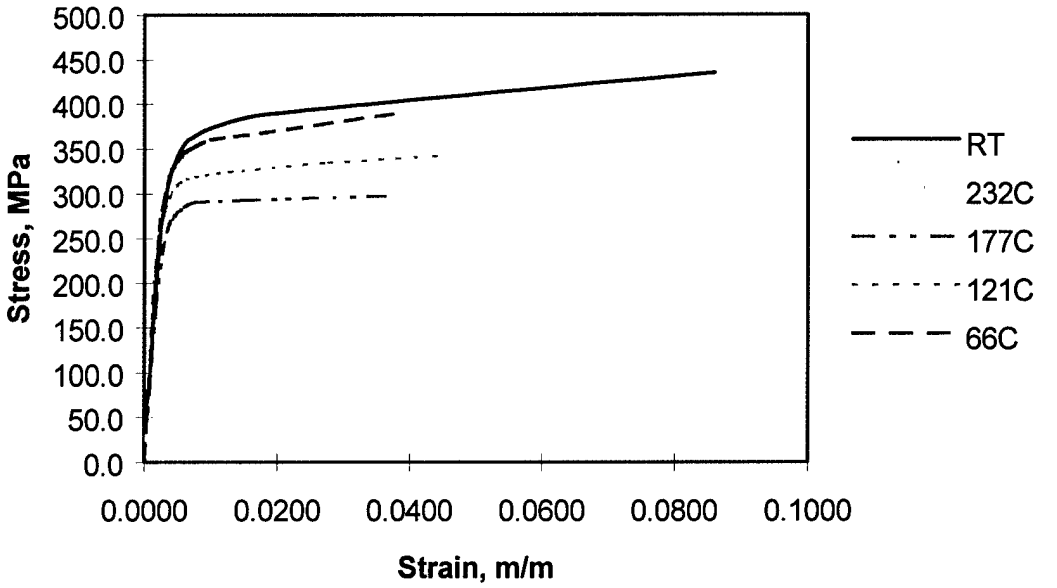

Figure 2. Stress-strain curves for wrought Be-Al alloy of L-orientation at various temperatures.

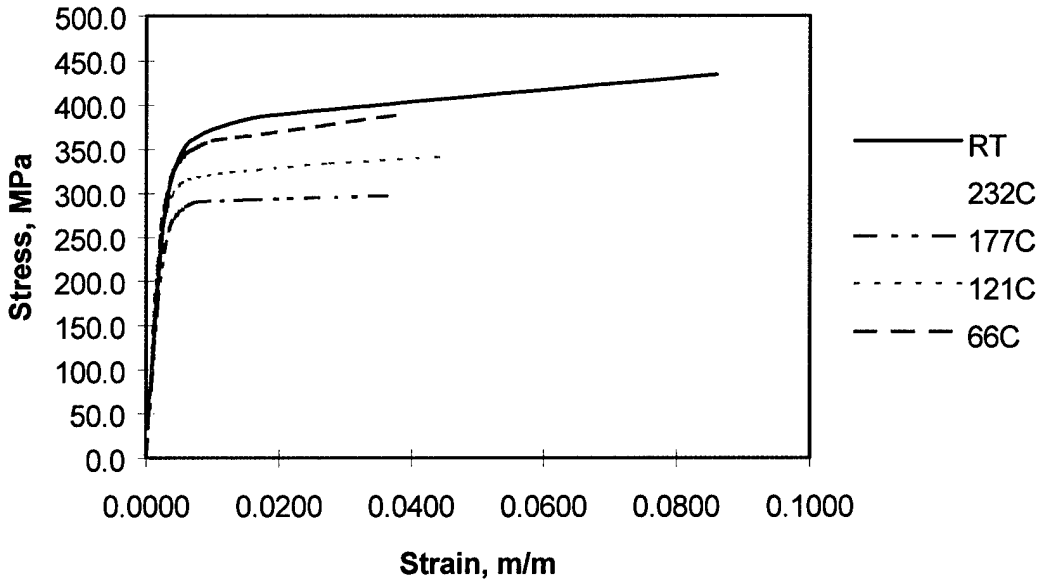

Figure 3. Stress-strain curves for wrought Be-Al alloy of T-orientation at various temperatures.

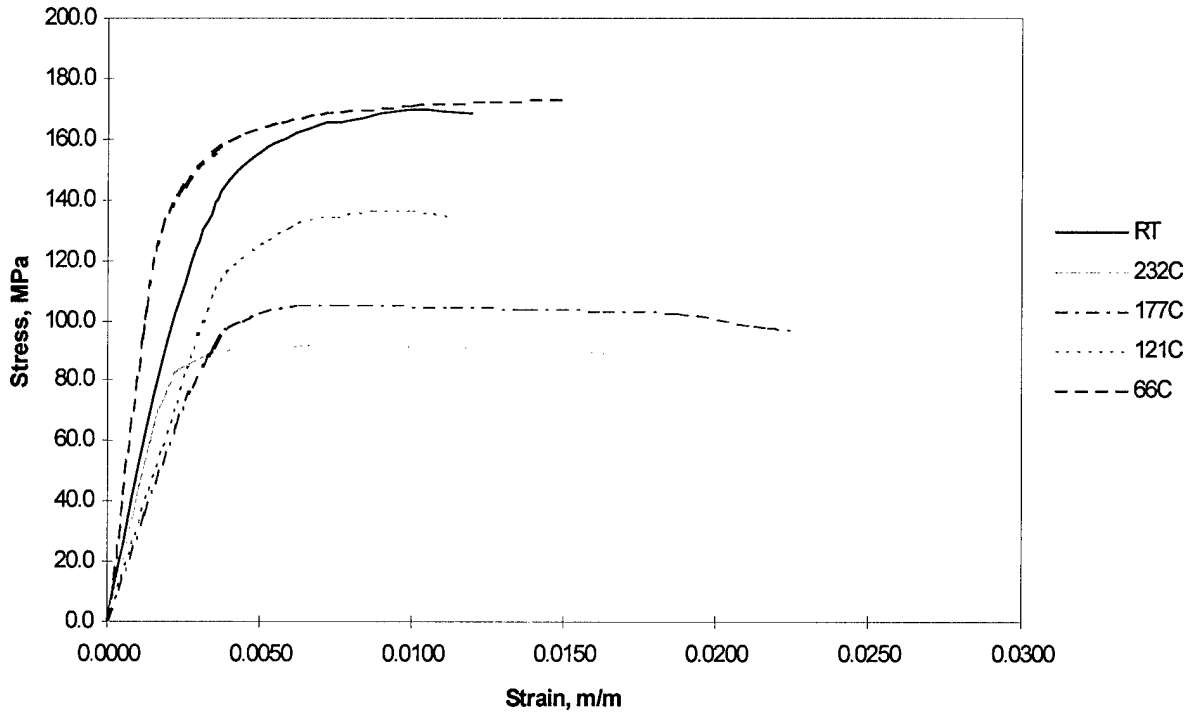

Figure 4. Stress-strain curves for cast Be-Al alloy at various temperatures.

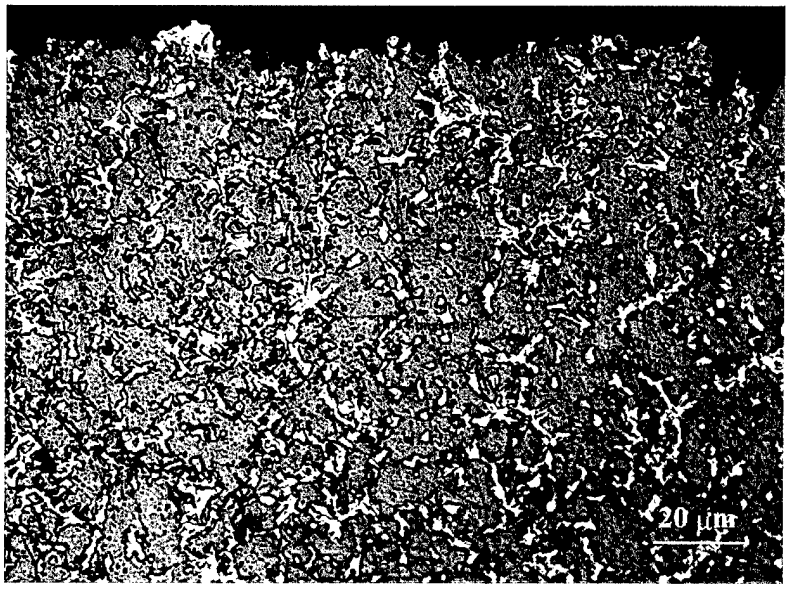

Figure 5. Optical micrograph of a longitudinal section through the fracture surface showing the fracture path and microstructure for a wrought Be-Al alloy specimen that had been tensile tested at room temperature.

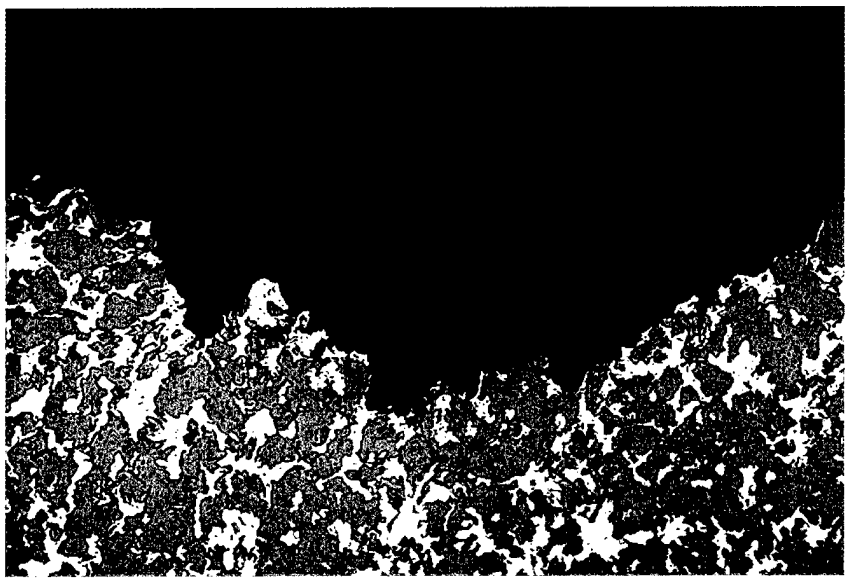

Figure 6. Optical micrograph of a longitudinal section through the fracture surface showing the fracture path and microstructure for a wrought Be-Al alloy specimen tensile tested at 232°C (450°F).

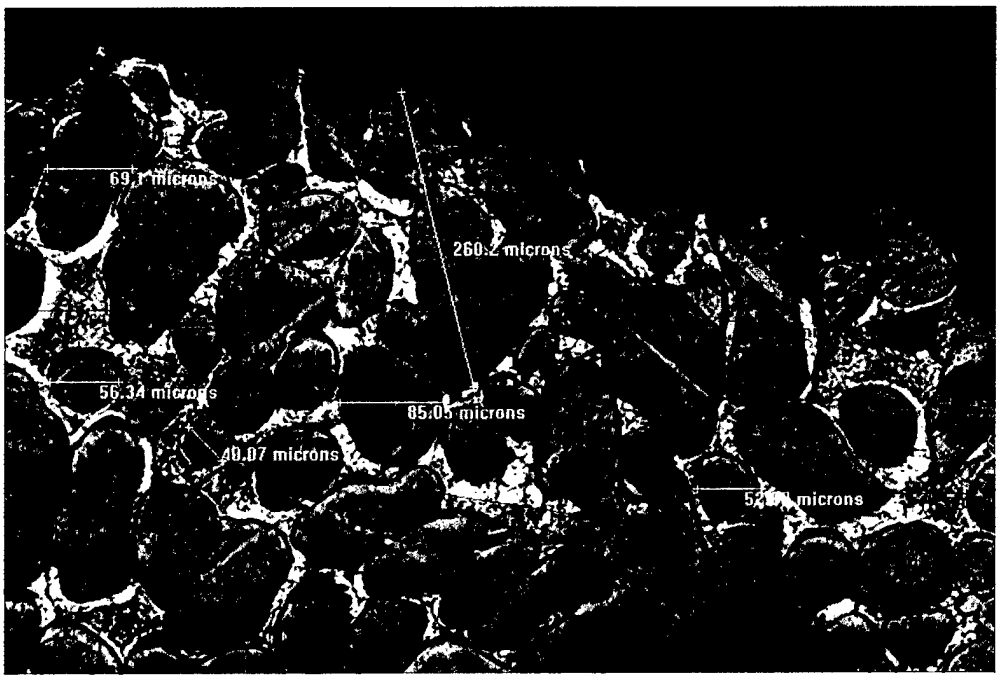

Figure 7. Optical micrograph of a section through the fracture surface showing the fracture path and microstructure for a cast Be-Al alloy specimen tensile tested at room temperature.

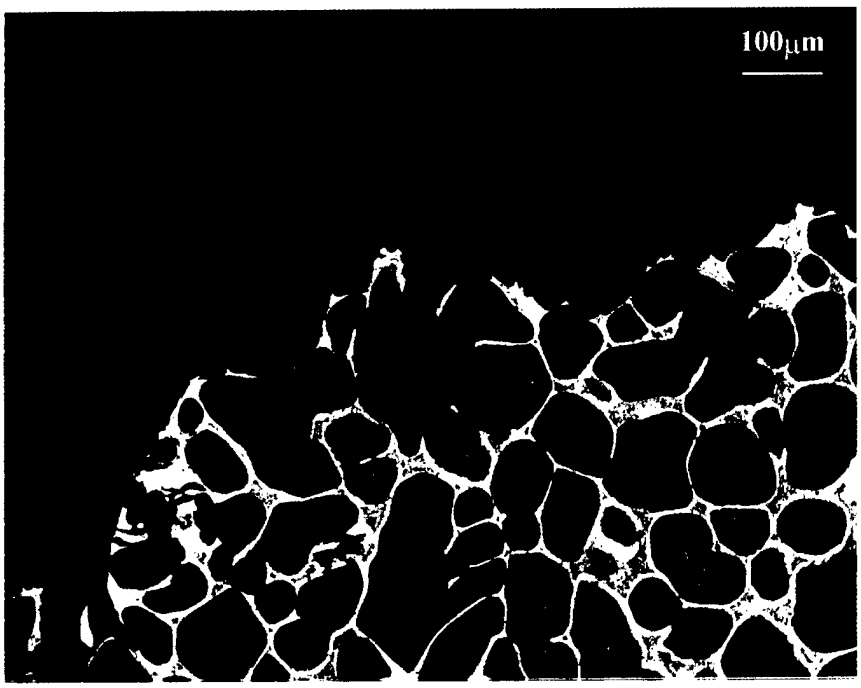

Figure 8. Optical micrograph of a section through the fracture surface showing the fracture path and microstructure for a cast Be-Al alloy specimen tensile tested at 232°C (450°F).

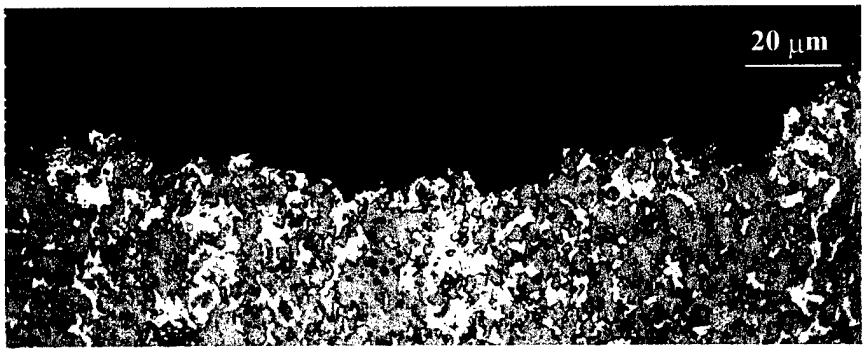

Figure 9. Optical micrographs of a section through the fracture surface showing the fracture path and microstructure for a wrought Be-Al alloy specimen of L-T orientation that had been fracture-toughness tested at room temperature.

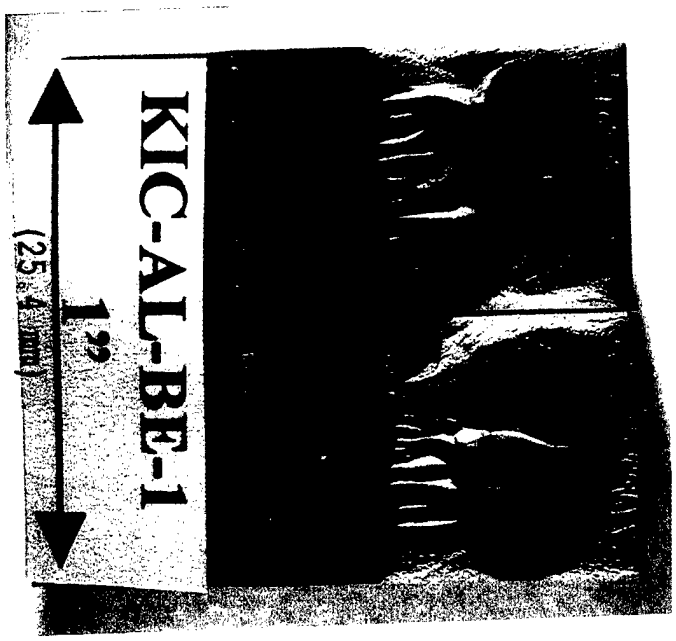

(a) L-T orientation

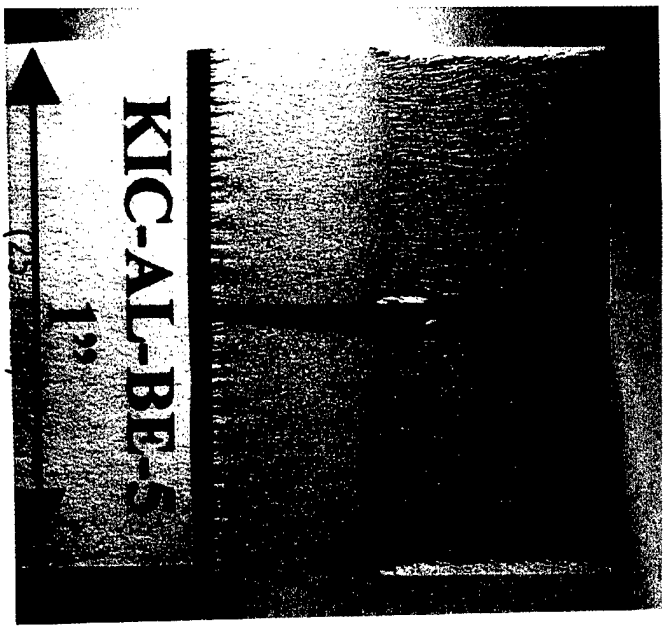

(b) T-L orientation

Figure 10. Photographs depicting the fracture surfaces of a wrought Be-Al alloy specimen that was fracture-toughness tested at room temperature.

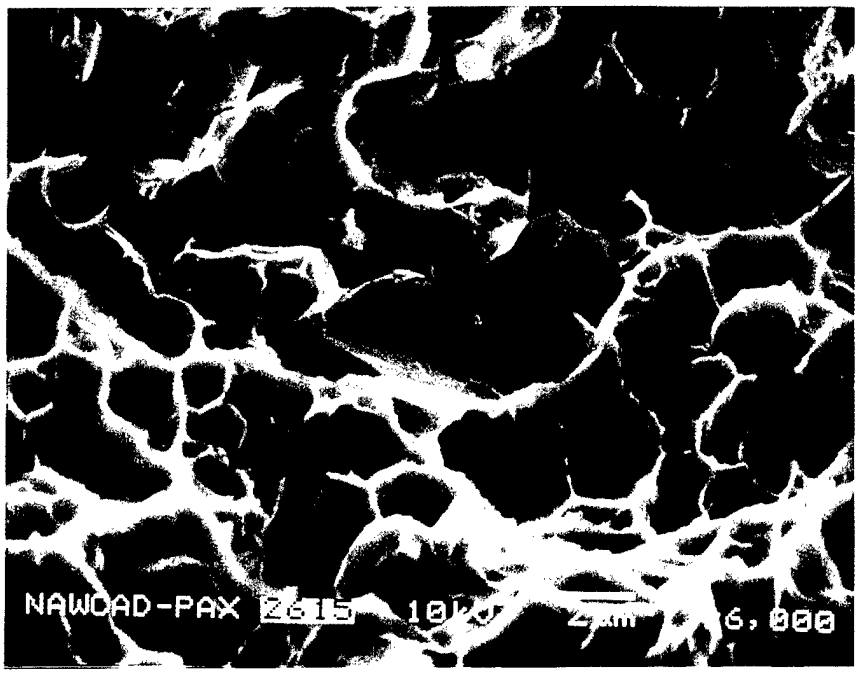

(a) SEM fractograph

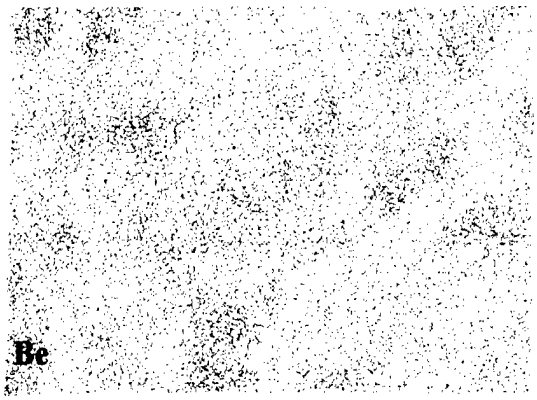

(b) X-ray dot mapping of Be

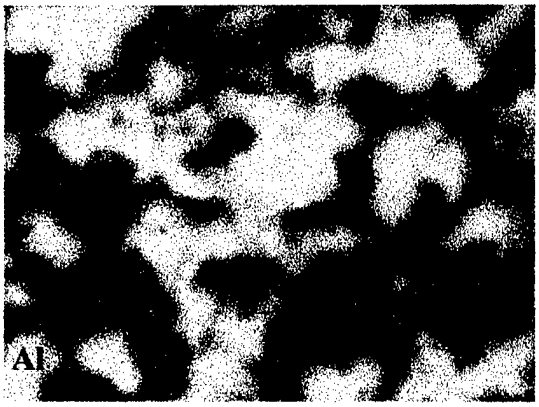

(c) X-ray dot mapping of Al

Figure 11. SEM micrograph and X-ray dot maps for a wrought Be-Al alloy specimen of L-T orientation that had been fracture-toughness tested at room temperature.

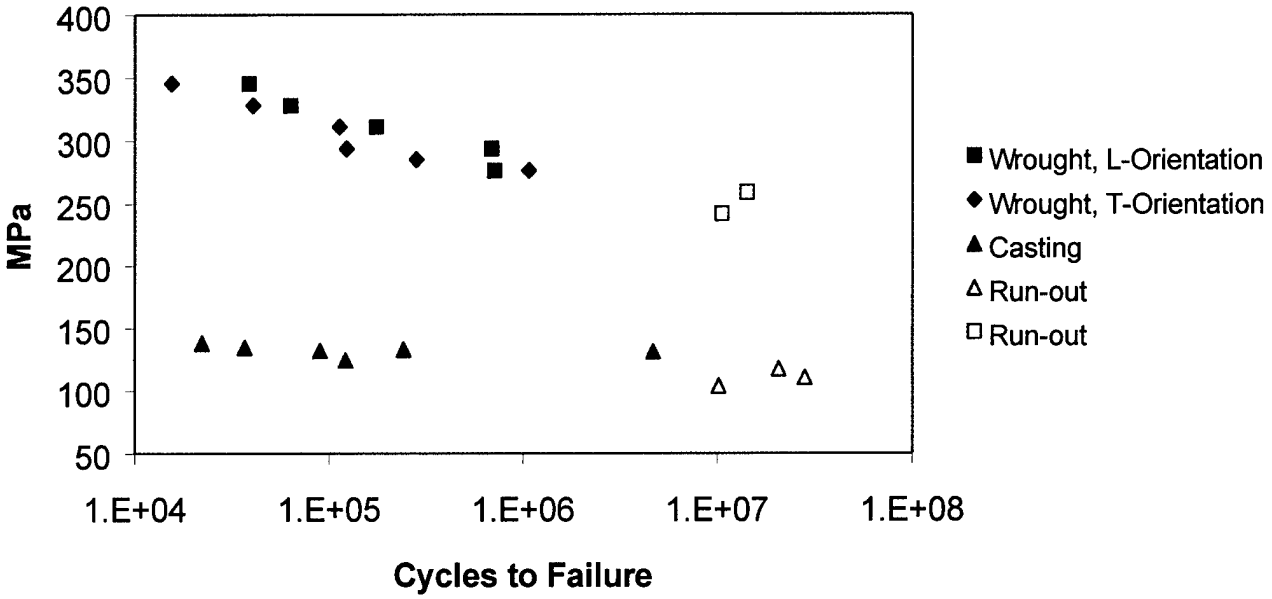

Figure 12. Stress-life (S-N) curves for wrought and cast Be-Al alloys that were fatigue tested at room temperature.

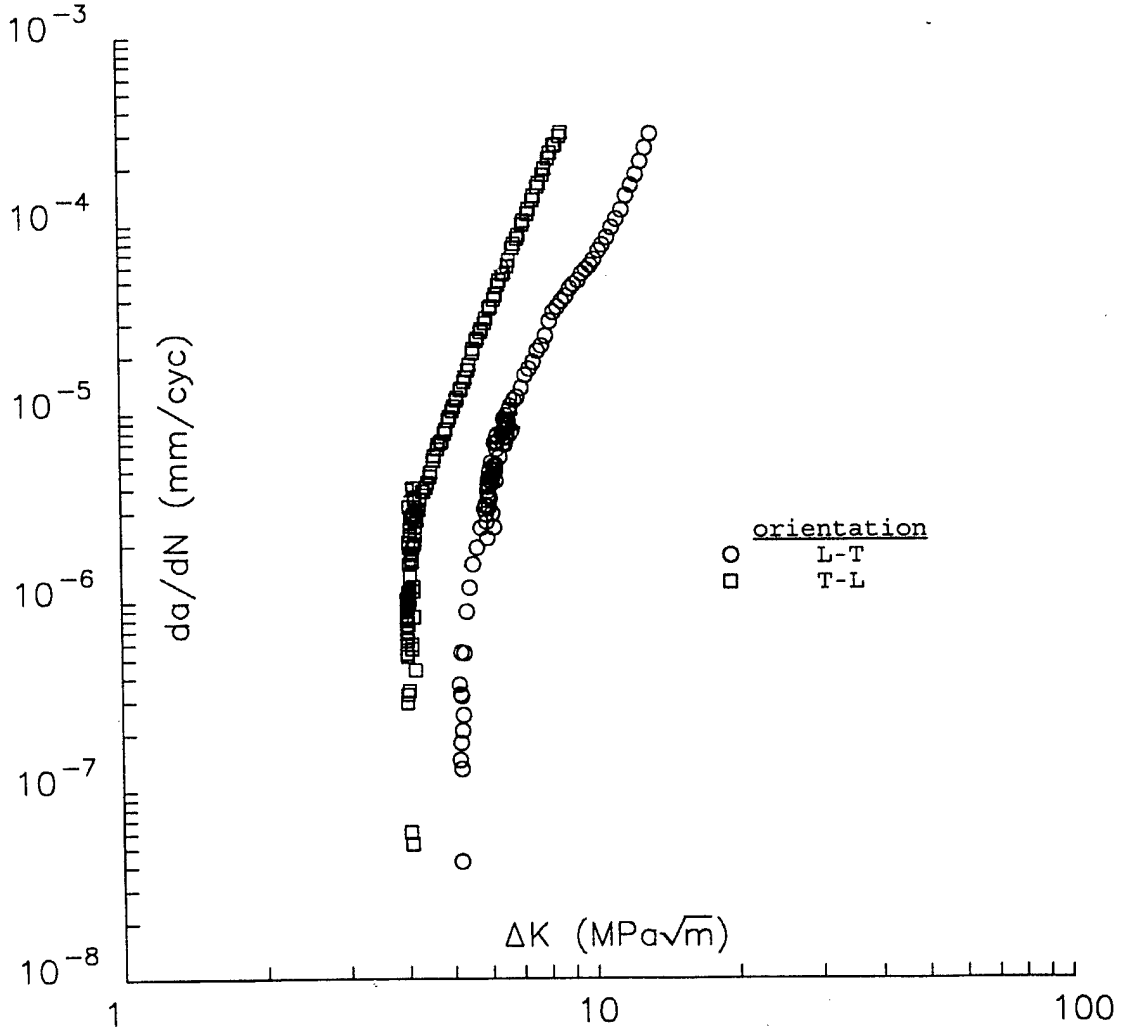

Figure 13. Variation of fatigue crack growth rate da/dN with stress intensity range ΔK for wrought Be-Al alloy specimens of L-T and T-L orientations at a stress ratio R = 0.1.

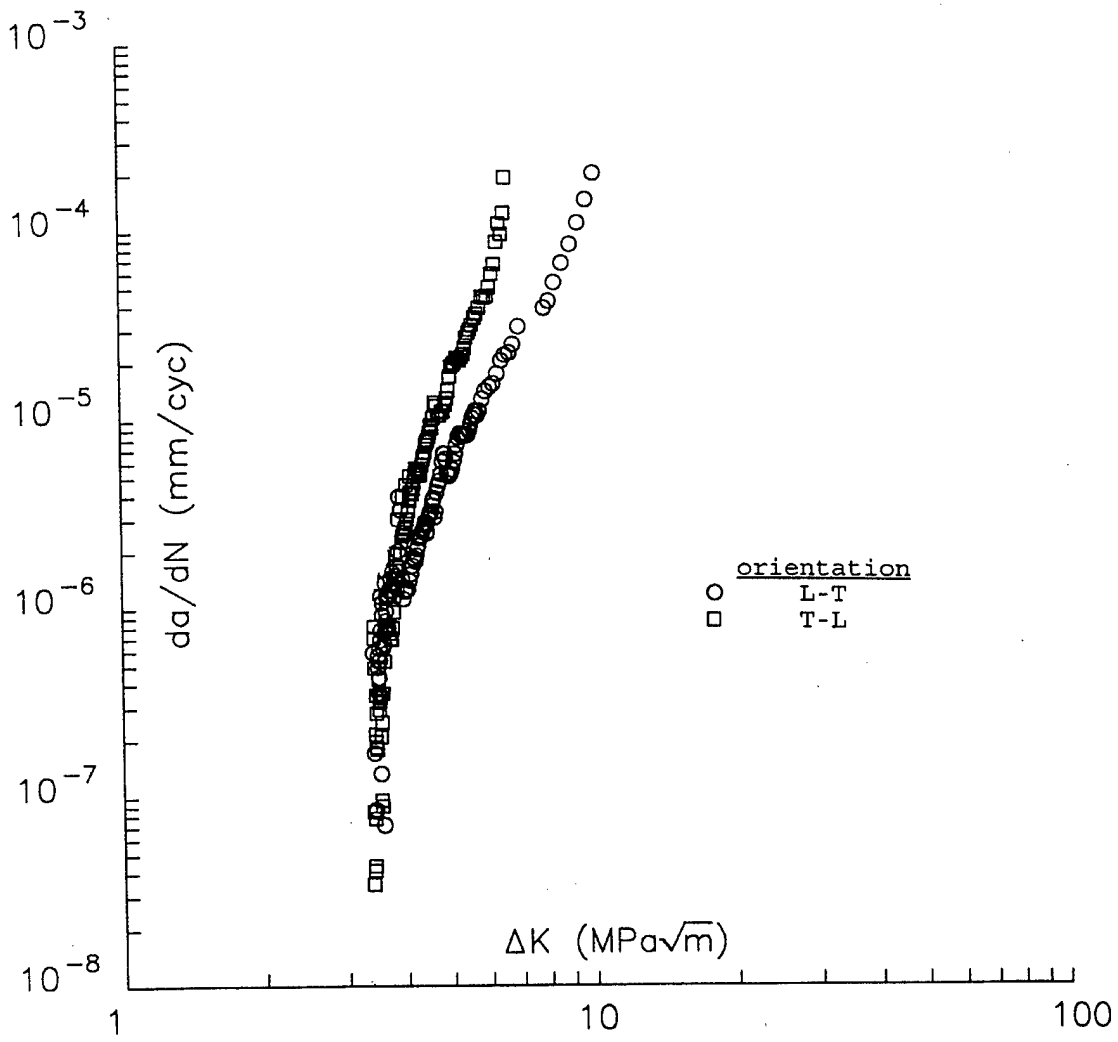

Figure 14. Variation of fatigue crack growth rate da/dN with stress intensity range ΔK for wrought Be-Al alloy specimens of L-T and T-L orientations at a stress ratio R = 0.6.

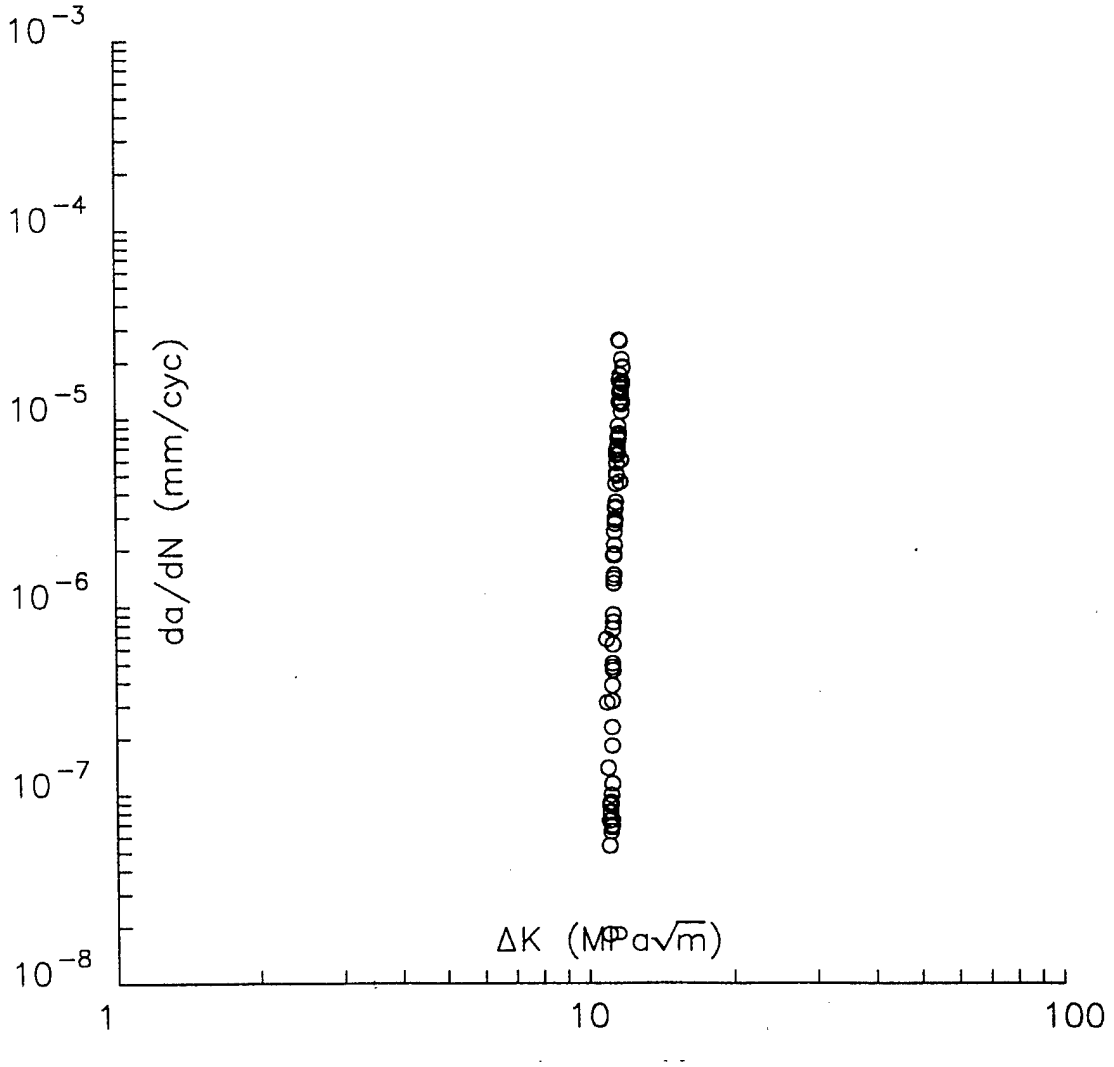

Figure 15. Variation of fatigue crack growth rate da/dN with stress intensity range ΔK for a cast Be-Al alloy specimen at a stress ratio R = 0.1.

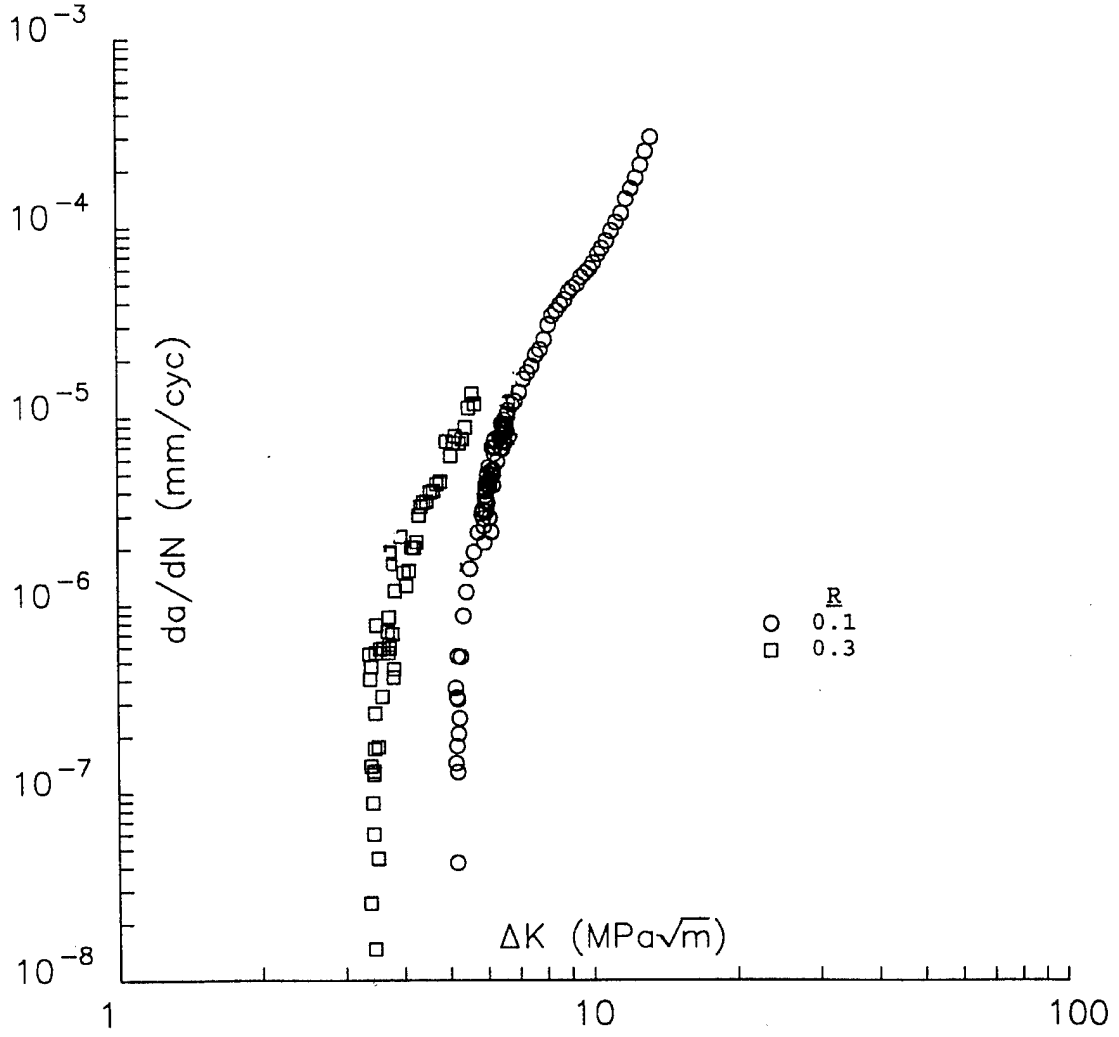

Figure 16. Variation of fatigue crack growth rate da/dN with stress intensity range ΔK for wrought Be-Al alloy specimens of L-T orientation at stress ratios R = 0.1 and 0.3.

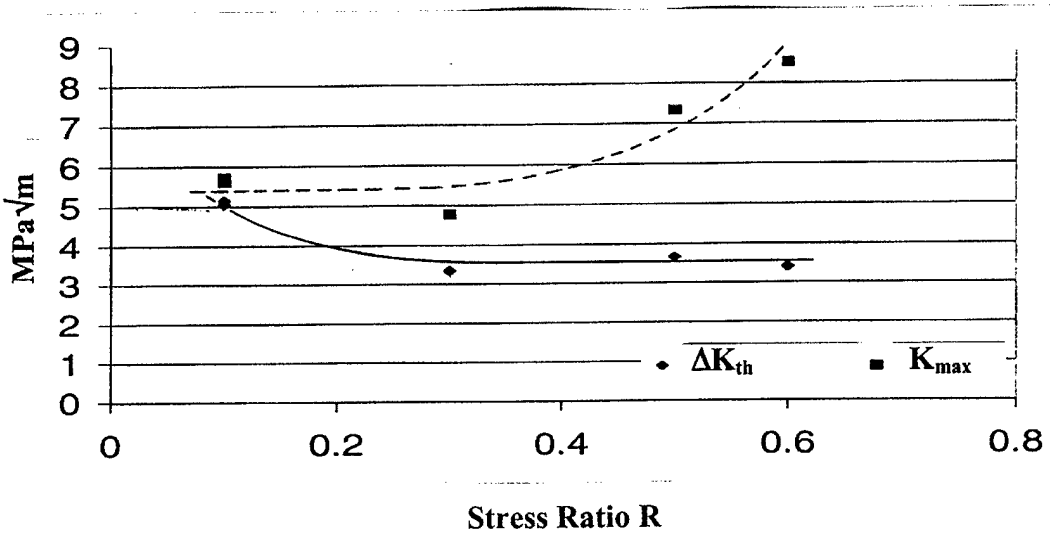

Figure 17. Variation of threshold stress intensity range ΔK and maximum stress intensity K_{max} with stress ratio R for wrought Be-Al alloy specimens of L-T orientation.

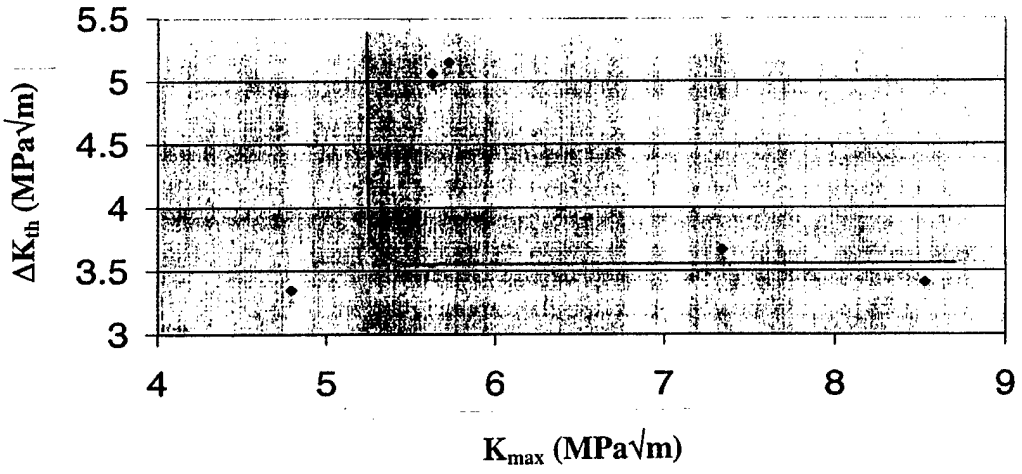

Figure 18. Fundamental threshold curve of threshold stress intensity range ΔK and maximum stress intensity K_{max} for wrought Be-Al alloy specimens of L-T orientation.

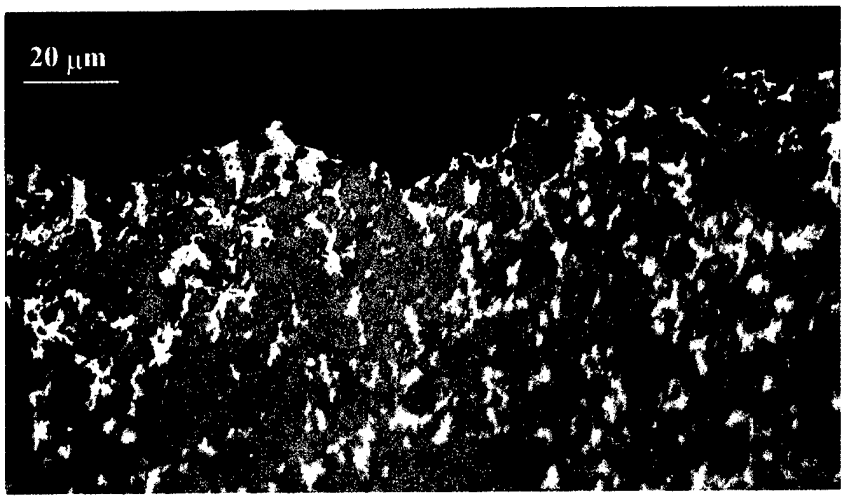

(a) L-orientation

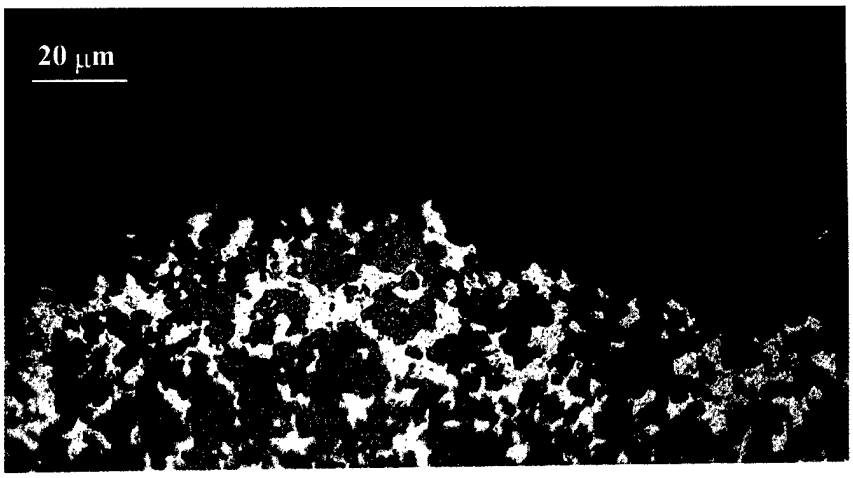

(b) T-orientation

Figure 19. Optical micrographs of a section through the fracture surface displaying the fracture path and microstructure for wrought Be-Al alloy specimens of L-T orientation that had undergone fatigue testing at room temperature.

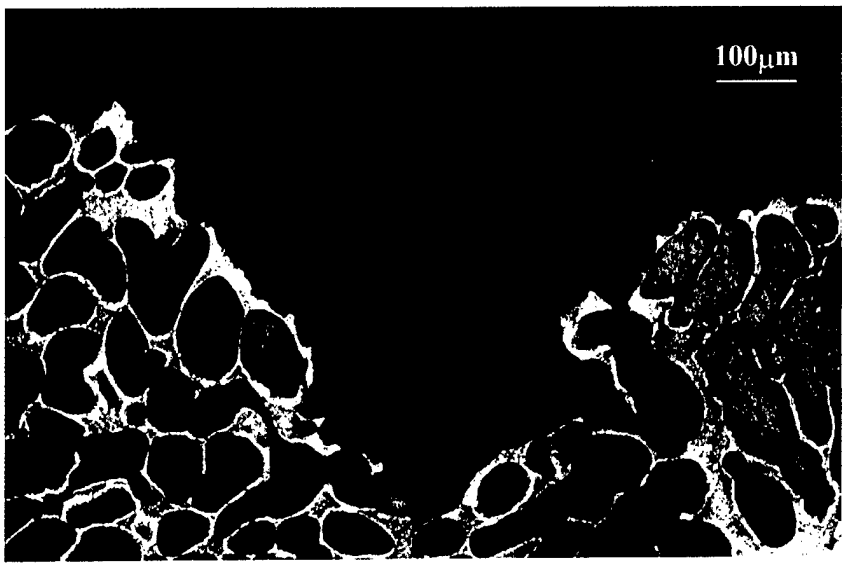

Figure 20. Optical micrograph of a section through the fracture surface depicting the fracture path and microstructure for a cast Be-Al alloy specimen that had undergone fatigue testing at room temperature.

REPORT DOCUMENTATION PAGE

Form Approved
OMB No. 0704-0188

1. REPORT DATE	2. REPORT TYPE	3. DATES COVERED
	Professional Paper	

4. TITLE AND SUBTITLE

Mechanical Behavior of Be-Al Alloys

5a. CONTRACT NUMBER

5b. GRANT NUMBER

5c. PROGRAM ELEMENT NUMBER

6. AUTHOR(S)

E. U. Lee K. A. George V. V. Agarwala
H. Sanders G. London

5d. PROJECT NUMBER

5e. TASK NUMBER

5f. WORK UNIT NUMBER

7. PERFORMING ORGANIZATION NAME(S) AND ADDRESS(ES)

Naval Air Warfare Center Aircraft Division
22347 Cedar Point Road, Unit #6
Patuxent River, Maryland 20670-1161

8. PERFORMING ORGANIZATION REPORT NUMBER

9. SPONSORING/MONITORING AGENCY NAME(S) AND ADDRESS(ES)

Naval Air Systems Command
47123 Buse Road Unit IPT
Patuxent River, Maryland 20670-1547

10. SPONSOR/MONITOR'S ACRONYM(S)

11. SPONSOR/MONITOR'S REPORT NUMBER(S)

12. DISTRIBUTION/AVAILABILITY STATEMENT

Approved for public release; distribution is unlimited.

13. SUPPLEMENTARY NOTES

14. ABSTRACT

This study was conducted to identify the mechanical behavior of a wrought 62Be-38Al alloy and a cast 65Be-32AL-3Ni alloy. Tensile strength and elongation were measured at room and elevated temperatures. Fracture toughness was determined at room temperature. Fatigue resistance was characterized in terms of stress-life (S-N) and crack growth rate-stress intensity range (da/dN-ΔK) relations at room temperature. The resulting microstructures and crack paths of the aforementioned were also examined.

15. SUBJECT TERMS

Be-Al Alloys Mechanical Behavior

16. SECURITY CLASSIFICATION OF:			17. LIMITATION OF ABSTRACT	18. NUMBER OF PAGES	19a. NAME OF RESPONSIBLE PERSON
a. REPORT	b. ABSTRACT	c. THIS PAGE			E. U. Lee / K. A. George
					19b. TELEPHONE NUMBER (include area code)
Unclassified	Unclassified	Unclassified	Unclassified	26	(301) 342-8069 / 342-8022

Standard Form 298 (Rev. 8-98)
Prescribed by ANSI Std. Z39-18